

Privacy-Preserving Federated Foundation Model for Generalist Ultrasound Artificial Intelligence

Yuncheng Jiang^{1,2,3,5,*}, Chun-Mei Feng^{3,*}, Jinke Ren^{1,2}, Jun Wei⁴, Zixun Zhang^{1,2}, Yiwen Hu⁶, Yunbi Liu⁷, Rui Sun^{1,2}, Xuemei Tang⁸, Juan Du⁹, Xiang Wan⁵, Yong Xu¹⁰, Bo Du¹¹, Xin Gao^{12,13}, Guangyu Wang¹⁴, Shaohua Zhou^{15,16}, Shuguang Cui^{2,1}, Rick Siow Mong Goh³, Yong Liu^{3,‡}, and Zhen Li^{2,1,‡,†}

¹FNii-Shenzhen, The Chinese University of Hong Kong (Shenzhen), Shenzhen 518172, China

²School of Science and Engineering, The Chinese University of Hong Kong (Shenzhen), Shenzhen 518172, China

³Institute of High Performance Computing, Agency for Science, Technology and Research, Singapore 138632, Singapore

⁴College of Computer Science and Software Engineering, Shenzhen University, Shenzhen 518060, China

⁵Shenzhen Research Institute of Big Data, Shenzhen 518172, China

⁶South China Hospital, Health Science Center, Shenzhen University, Shenzhen 518111, China

⁷School of Computer Science, Nanjing University of Posts and Telecommunications, Nanjing 210023, China

⁸Affiliated Hospital of North Sichuan Medical College, Sichuan 637000, China

⁹North Sichuan Medical College, Sichuan 637000, China

¹⁰Bio-Computing Research Center, Harbin Institute of Technology (Shenzhen), Shenzhen 518055, China

¹¹School of Computer Science, Wuhan University, Wuhan 430072, China

¹²Computer Science Program, Computer, Electrical and Mathematical Sciences and Engineering Division, King Abdullah University of Science and Technology (KAUST), Thuwal 23955-6900, Kingdom of Saudi Arabia.

¹³Center of Excellence for Smart Health (KCSH), King Abdullah University of Science and Technology (KAUST), Thuwal 23955-6900, Kingdom of Saudi Arabia.

¹⁴Beijing University of Posts and Telecommunications, Beijing 100876, China

¹⁵School of Biomedical Engineering, Suzhou Institute for Advanced Research, University of Science and Technology of China, Suzhou 215123, China

¹⁶Institute of Computing Technology, Chinese Academy of Sciences, Beijing 100190, China

*The authors contributed equally to this work.

‡Equal last authors.

†Corresponding authors: Zhen Li (e-mail: lizhen@cuhk.edu.cn)

ABSTRACT

Ultrasound imaging is widely used in clinical diagnosis due to its non-invasive nature and real-time capabilities. However, conventional ultrasound diagnostics face several limitations, including high dependence on physician expertise and suboptimal image quality, which complicates interpretation and increases the likelihood of diagnostic errors. Artificial intelligence (AI) has emerged as a promising solution to enhance clinical diagnosis, particularly in detecting abnormalities across various biomedical imaging modalities. Nonetheless, current AI models for ultrasound imaging face critical challenges. *First*, these models often require large volumes of labeled medical data, raising concerns over patient privacy breaches. *Second*, most existing models are task-specific, which restricts their broader clinical utility. To overcome these challenges, we present **UltraFedFM**, an innovative privacy-preserving ultrasound foundation model. UltraFedFM is collaboratively pre-trained using federated learning across 16 distributed medical institutions in 9 countries, leveraging a dataset of over 1 million ultrasound images covering 19 organs and 10 ultrasound modalities. This extensive and diverse data, combined with a secure training framework, enables UltraFedFM to exhibit strong generalization and diagnostic capabilities. It achieves an average area under the receiver operating characteristic curve (AUROC) of 0.927 for disease diagnosis and a dice similarity coefficient (DSC) of 0.878 for lesion segmentation. Notably, UltraFedFM surpasses the diagnostic accuracy of mid-level ultrasonographers (4–8 years of experience) and matches the performance of expert-level sonographers (10+ years of experience) in the joint diagnosis of 8 common systemic diseases. These findings indicate that UltraFedFM can significantly enhance clinical diagnostics while safeguarding patient privacy, marking a significant advancement in AI-driven ultrasound imaging for future clinical applications.

Introduction

Ultrasound is becoming increasingly important in clinical practice worldwide. It offers significant advantages over magnetic resonance imaging (MRI) and computed tomography (CT), including freedom from radiation, non-invasive nature, and cost-effectiveness. Thus, it is widely adopted as the primary imaging method for monitoring fetal growth during pregnancy¹, diagnosing internal organ pathology, and assisting in surgical decision-making². However, ultrasound-based diagnosis relies heavily on the clinician's experience, while factors like noise and artifacts in the images can compromise quality and hinder the clinician's assessment of pathological regions, increasing the risk of missed or incorrect diagnoses^{3,4}. Recent efforts have turned to artificial intelligence (AI) technologies to enhance diagnostic accuracy⁵⁻⁷. Despite notable successes, existing AI-based ultrasound models typically focus on very specific medical scenarios and require large amounts of high-quality labeled data, which restricts their scalability and generalizability across diverse medical applications.

Over the past two years, foundational models (FMs) have attracted much attention due to their generality and high performance. In the medical field, many efforts^{8,9} have leveraged unlabeled ultrasound data to pre-train FMs and fine-tuned them for specific tasks using labeled data. However, existing ultrasound foundational models (USFMs) face three key challenges: (1) **Data privacy**. Ultrasound data are distributed across multiple medical institutions and cannot be shared due to privacy regulations (e.g., GDPR¹⁰), restricting the volume of data available for pre-training; (2) **Limited modality**. Many USFMs are designed for particular ultrasound imaging modalities (e.g., echocardiograms), limiting their applicability to other imaging modalities and reducing their versatility; (3) **Imbalanced data distribution**. Existing USFMs often face an imbalance caused by the long-tailed distribution of the organ/lesion types represented in the dataset (e.g., 91% breast ultrasound in 3M-US⁸), leading to a biased performance in diagnosing uncommon conditions. These challenges highlight the need for new solutions that simultaneously address data privacy, scalability, and generalizability across various ultrasound imaging modalities and clinical scenarios.

In this work, we introduce UltraFedFM, a novel ultrasound foundation model pre-trained collaboratively by multiple medical institutions without exposing and aggregating all the data together. Specifically, we utilize a federated learning framework with one server and 16 clients from 9 countries, collectively possessing 1,015,754 unlabeled ultrasound images (Fig. 1a). These images cover 19 systemic organs and 10 ultrasound imaging modalities (Fig. 2a-b), providing extensive and diverse representation for pre-training. The development of UltraFedFM consists of two stages: (1) Federated pre-training, in which the multiple clients collaboratively pre-train a shared model in a distributed, self-supervised manner. Throughout the pre-training process, the server periodically aggregates the local model parameters from each client without accessing their private data (Fig. 1b); (2) Downstream fine-tuning, where the pre-trained FM is fine-tuned using specific data to adapt to various clinical tasks, such as disease screening and diagnosis, sub-classification of disease phenotypes (e.g., tumor infiltration depth and type classification), prenatal maternal-fetal health analysis, and critical lesion identification and segmentation (Fig. 1c).

UltraFedFM is adapted to various ultrasound imaging modalities, modes, qualities, and clinical tasks. To accommodate the diverse features of different modalities, we propose a dynamic ultrasound image masking approach based on the specific texture features of organs and lesions. Additionally, we incorporate a random image corruption branch within the masked image modeling process to handle low-quality images commonly encountered in real-world scenarios. Furthermore, we use simple yet effective image transformations to generate simulated ultrasound images, aiming to address the uneven distribution of scan patterns in the pre-training dataset (see Method for details).

We conduct extensive experiments to evaluate the performance of UltraFedFM. To provide a fair and comprehensive evaluation, we collect and curate the largest ultrasound evaluation benchmark, covering the two most common ultrasound clinician tasks (i.e., disease diagnosis and lesion segmentation) with 11 sub-tasks from 19 ultrasound datasets. Several fully-supervised methods and a state-of-the-art USFM⁸ are utilized for comparison. Experimental results demonstrate that UltraFedFM outperforms all baselines, achieving an average area under the curve (AUROC) of 0.927 for disease diagnosis and a dice similarity coefficient (DSC) of 0.878 for lesion segmentation. Notably, UltraFedFM outperforms ultrasonographer clinicians with intermediate levels (e.g., 4-8 years of clinical experience) and achieves comparable performance to high-level (e.g., more than 10 years of clinical experience) ultrasonographers in the joint diagnosis of 8 common systemic diseases. Moreover, we perform a thorough investigation to demonstrate the generalizability of UltraFedFM to new modalities, its stability against input perturbations, and its interoperability. With these capabilities, UltraFedFM provides a reliable model for clinical tasks, making it a pioneering solution for advancing ultrasound AI across institutions, regions, and clinical tasks.

Results

UltraFedFM enables systemic disease diagnosis

UltraFedFM aims to serve as a comprehensive FM in ultrasound imaging. To assess its effectiveness for disease diagnosis, 6 publicly available datasets and 2 private datasets (see Table 2) are utilized, covering 8 kinds of organs (i.e., pancreas, gallbladder, liver, lung, colorectum, breast, heart, and fetal organs, see Fig. 10) and 6 ultrasound imaging modalities (i.e., abdominal, lung,

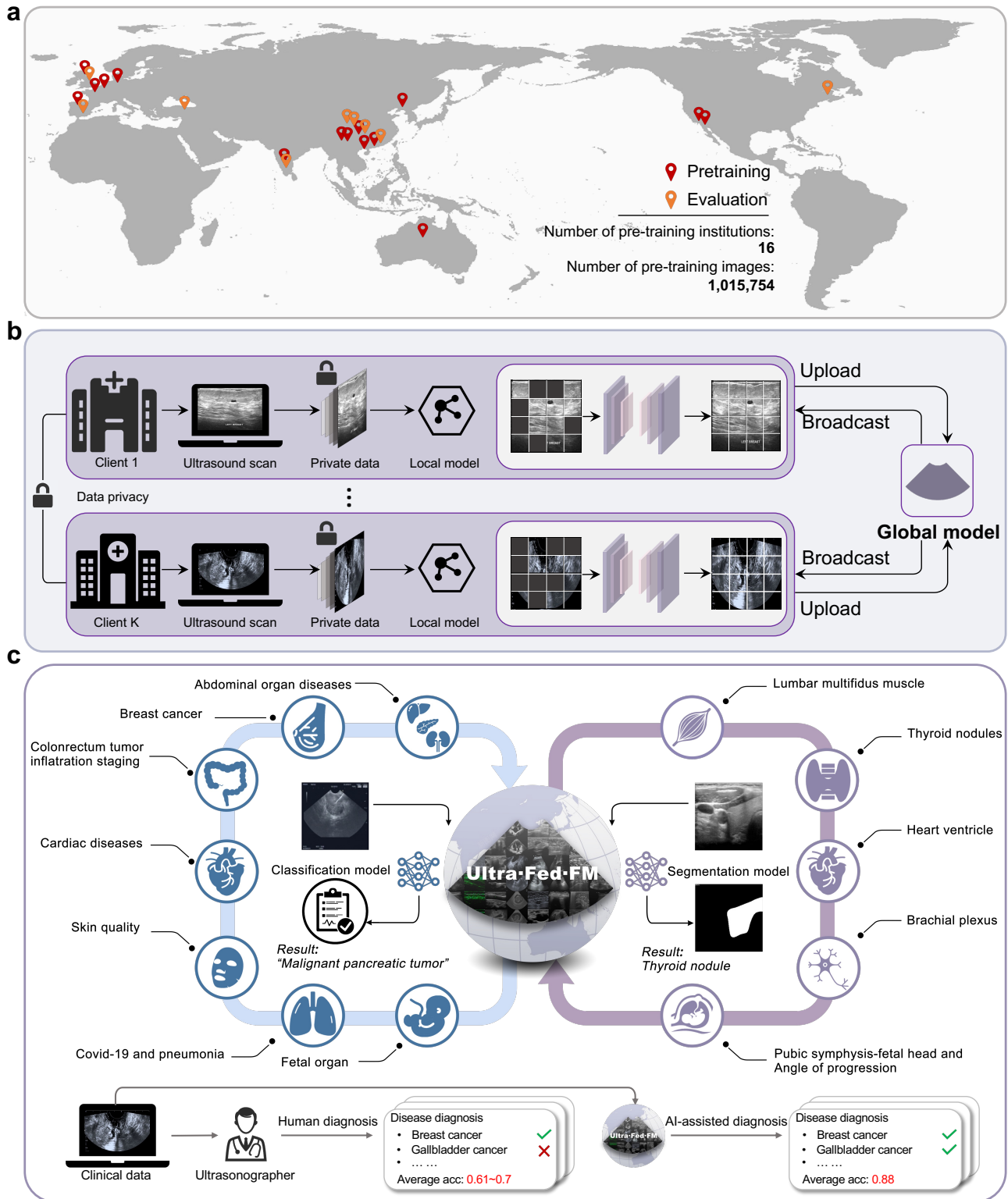


Figure 1. Dataset, pre-training framework, and clinical applications of UltraFedFM. **a** Medical data from 16 institutions and 9 countries are collected to pre-train and evaluate UltraFedFM, encompassing 1 million ultrasound images with extensive diversity. **b** The pre-training framework of UltraFedFM, where each client uses its private data to pre-train a local model through pixel-level reconstruction. During pre-training, only the local model parameters are uploaded for learning the global model, thus eliminating the risk of privacy breaches. **c** Clinical applications of UltraFedFM. UltraFedFM is a versatile ultrasound foundation model capable of handling multiple ultrasound scenarios, supporting multi-disease, multi-modal, and multi-task applications, and demonstrating superior performance compared with ultrasonographers in real clinical scenarios.

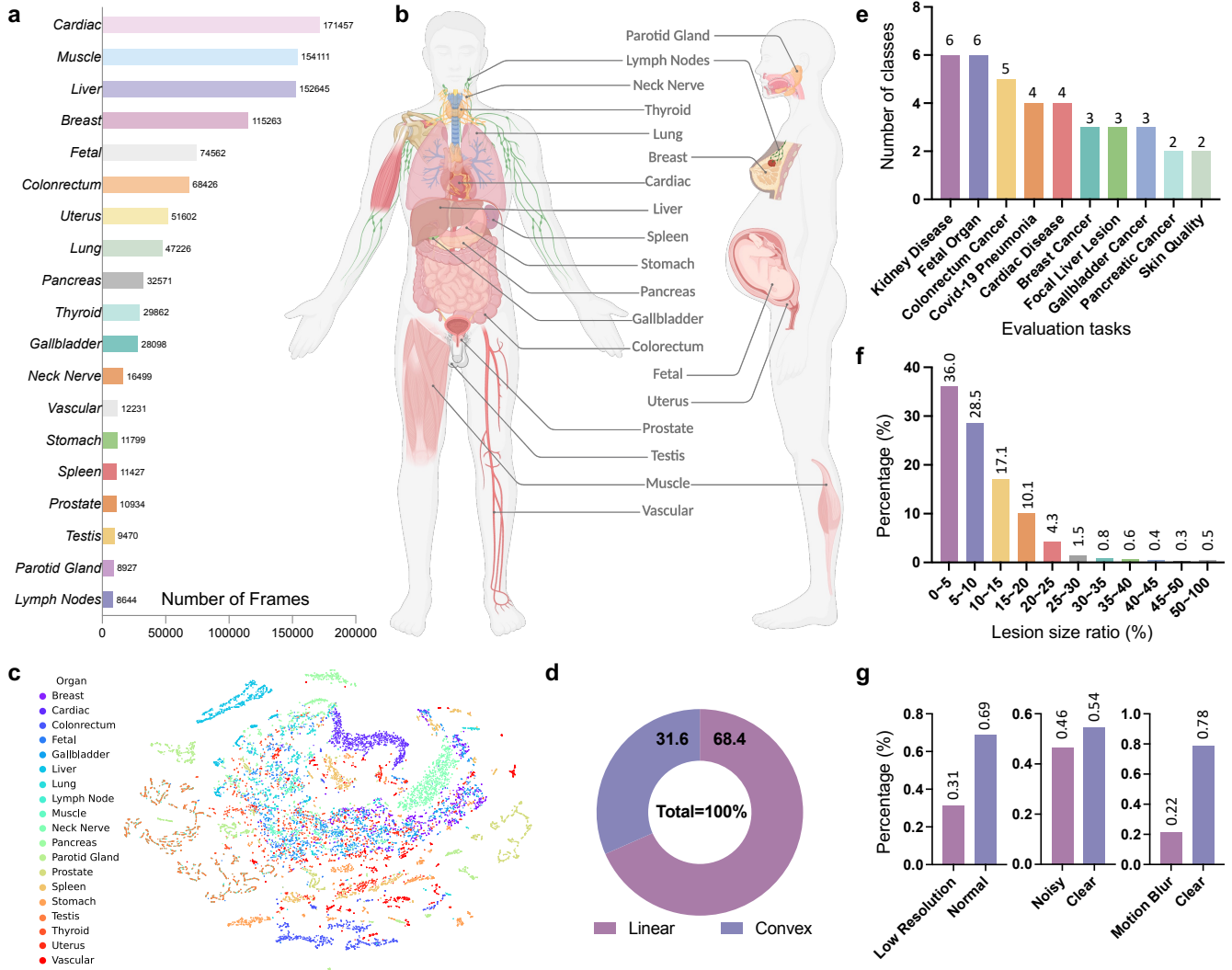


Figure 2. Statistics of the pre-training and downstream validation datasets. **a-b** The pre-training dataset covers 19 major organs across the entire body captured by various ultrasound imaging modalities. **a** shows the specific types of organs and their quantitative distribution, while **b** displays their locations in the human body. **c** Visualization of the tSNE distribution of 19 organ features in two-dimensional feature space after dimensionality reduction. **d** The distribution of scanning modes in the pre-training dataset. **e** The downstream validation dataset includes 10 common systemic disease diagnosis tasks, ranging from basic binary classification to complex multi-class classification. **f** The distribution of the target size for organ and lesion segmentation tasks in the downstream validation dataset. Most segmentation targets occupy less than 1/10 of the entire image. **g** The distribution of different types of low-quality ultrasound images in the downstream validation dataset that hinders clinical judgment, including low resolution, motion blur, and noise.

endorectal, superficial, echocardiogram, and fetal ultrasound). To provide an overall assessment for UltraFedFM, we average its performance on these datasets, and compare it with 4 baseline methods, including supervised training from scratch, ImageNet-21k centralized pre-training, USFM⁸ centralized pre-training, and masked autoencoder (MAE)¹¹ federated pre-training. More details of the four methods are described in the Method section. The experimental results are shown in Fig. 3. We observe that UltraFedFM achieves an average AUROC of 0.927, which significantly ($p < 0.05$) outperforms its counterparts, surpassing the second-best USFM with an average AUROC of 0.894, by 0.033 ($p = 0.002$). Additionally, UltraFedFM performs well in data-limited situations (see line charts in Fig. 3a). As the amount of fine-tuning data is progressively reduced to 80%, 60%, 40%, and 20%, UltraFedFM remains robust, with only a modest decline in average AUROC of 0.124 (fine-tuning data from 100% to 20%), outperforming other methods.

Due to the federated pre-training with the large volume of unlabeled data, UltraFedFM possesses powerful feature extraction capabilities and can identify various types of lesions using a single organ-agnostic decoder, thus eliminating the need for

task-specific classifiers utilized in other FMs. To demonstrate this, we constructed an organ-agnostic dataset by combining eight distinct datasets from different organs and fine-tune UltraFedFM to recognize eight types of malignant tumors. It is observed that UltraFedFM accurately identifies most categories without requiring a separate classifier for each organ and the predicted scores of UltraFedFM concentrate in higher confidence intervals (Fig. 3b). Fig. 3c illustrates the receiver operating characteristic (ROC) curves among eight different diseases, showing that UltraFedFM achieves superior efficiency in organ-agnostic disease diagnosis. More quantitative results for UltraFedFM, including accuracy, F1-score, and ROC, are provided in Supplementary Fig. 11, Fig. 12, and Fig. 13.

UltraFedFM is comparable with ultrasonographers

To evaluate the reliability of UltraFedFM's generalist intelligence from the clinical practice perspective, we compare it with ultrasonographers having different clinical levels. Seven ultrasonographers participated in this study, in which two of them are intermediate-level (clinicians A, B: 4-8 years of clinical experience) and five of them are high-level (clinicians C-G: more than 10 years of clinical experience). A total of 80 ultrasound images containing 8 systemic malignant diseases were tested. As shown in Fig. 3d and Table 5, UltraFedFM outperforms the ultrasonographers with intermediate-level and achieves comparable performance with high-level ultrasonographers. More specifically, while some specific organ diseases are easy for ultrasonographers to diagnose (e.g., average accuracy: 0.800 for breast and 0.871 for kidney), their diagnostic capabilities are limited when multiple ultrasound diseases are jointly diagnosed (e.g., average accuracy: 0.314 for gallbladder). In contrast, UltraFedFM can provide a consistent and accurate diagnosis of different ultrasound organ diseases (average accuracy: 0.900 for breast, 1.000 for kidney, and 0.800 for gallbladder). These results reveal that the UltraFedFM has the potential to serve as a reliable general intelligence to assist clinicians in the diagnostic process.

UltraFedFM facilitates organ and lesion segmentation

Organ and lesion segmentation for ultrasound images are crucial for clinical decision-making. To assess UltraFedFM's segmentation accuracy across different ultrasound imaging modalities, we evaluated it on four binary segmentation datasets (nerve¹², muscle¹³, heart¹⁴ and thyroid¹⁵⁻¹⁸) and one multi-class segmentation dataset (pubic symphysis-fetal head¹⁹). UltraFedFM consistently achieves high segmentation accuracy, successfully managing targets with diverse shapes and structures. In the binary segmentation task (Fig. 4a), UltraFedFM achieves the highest average dice similarity coefficient (DSC) score of 0.857 across the three binary segmentation datasets, significantly outperforming all other baselines ($p < 0.005$). In particular, USFM achieves a DSC score of 0.828, which is much lower than that of UltraFedFM ($p = 0.002$).

The multi-class segmentation task involves two steps beginning by segmenting the pubic symphysis and fetal head, followed by measuring the angle between them. In this task, UltraFedFM achieves a DSC score of 0.842, significantly outperforming the second-best method (USFM⁸) with a DSC score of 0.910 ($p = 0.004$). Additionally, UltraFedFM excels in measuring the angle of progression (AoP), with a mean absolute error of 8.80, outperforming all baselines by a significant margin ($p < 0.005$) (see Fig. 4a). Similar to the classification settings, we also evaluated UltraFedFM's effectiveness in scenarios with limited labeled data (see line charts in Fig. 4a). Notably, even with 20% of the fine-tuning data, UltraFedFM still achieves an average DSC score of 0.772, outperforming the supervised method and USFM by 14.0% and 2.3%, respectively. To further assess UltraFedFM's generalization capability, we compiled an organ-agnostic segmentation dataset comprising five types of lesions. As shown in Fig. 4b, UltraFedFM demonstrates superior performance in locating and segmenting these lesions using a single unified segmentation model.

In addition to evaluating UltraFedFM on datasets with similar distributions, we conducted cross-institutional evaluations by fine-tuning the model on one institutional dataset and testing it on others. UltraFedFM consistently outperforms other baselines in all cross-sets ($p < 0.01$), demonstrating superior stability and balanced generalization (see Fig. 4c). To enhance UltraFedFM's ability to recognize feature pairs from different scanning modes (i.e., linear-array and convex-array), we generated synthetic ultrasound imaging data via Polar-Cartesian transformation. Ablation studies were performed to quantify the impact of these synthetic images on UltraFedFM's learning outcomes. Fig. 4d illustrates the performance of UltraFedFM fine-tuned with different ratios of real to synthetic data. We observed that adding synthetic data generally enhances performance. This highlights the importance of balancing real and synthetic data, where the optimal performance is achieved at a 1:1 ratio.

The impact of SSL strategies on model performance

To validate the effectiveness of our modified masked autoencoder (MAE) strategy in UltraFedFM, we compare it with several baseline self-supervised learning (SSL) strategies, including vanilla MAE¹¹, SimCLR²⁰, SwAV²¹, DINO²², and MoCo²³. Fig. 5a-b shows that UltraFedFM with the modified MAE significantly outperforms all other baselines ($p < 0.001$) in both disease diagnosis and lesion segmentation tasks. Specifically, UltraFedFM achieves the highest average AUROC of 0.926 across eight classification tasks and an average DSC score of 0.878 across four segmentation tasks. In contrast, the vanilla MAE achieves the second-best performance, with an average AUROC of 0.884 and an average DSC score of 0.839. These results suggest that MAE-based approaches are more effective for ultrasound imaging than contrastive learning-based methods.

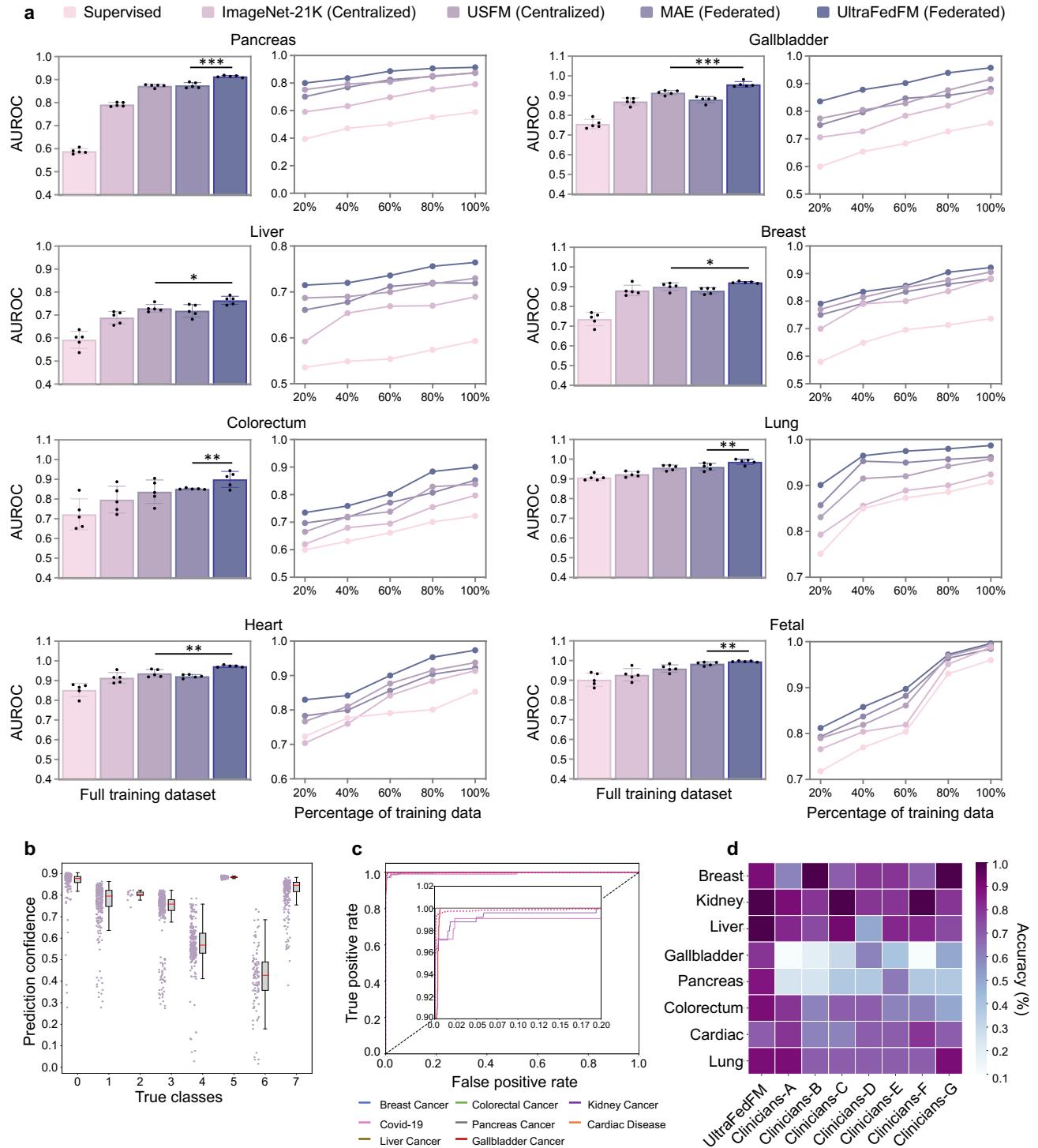


Figure 3. Performance on systemic disease diagnostic classification. **a** Internal evaluation on eight independent disease diagnosis tasks. The histogram is the models fine-tuned on the full data of each dataset, and the line chart is the models fine-tuned on part of the labeled data. For each task, we fine-tune the model with five different random seeds. The error bars show 95% confidence intervals (CI) of the estimates and the bar center is the mean estimate. We compare the performance using the area under the receiver operating characteristic curve (AUROC). P -value is calculated with the two-sided t-test among UltraFedFM and the most competitive comparison model. *, **, *** denotes $p < 0.05$, $p < 0.005$, and $p < 0.005$. **b-c** Performance of UltraFedFM on organ-agnostic fine-tuning setting, where **b** shows the prediction confidence distribution over eight classes. The center line of the box denotes the median, while the box edges represent the first and third quartiles and the whiskers extend to 1.5 times the inter-quartile range. The data distribution is shown alongside the box plot. **c** Area under the curve (AUC) of recognizing eight systemic malignant diseases. **d** Generalist diagnostic accuracy of UltraFedFM across eight diseases and the comparison with seven experienced ultrasonographers.

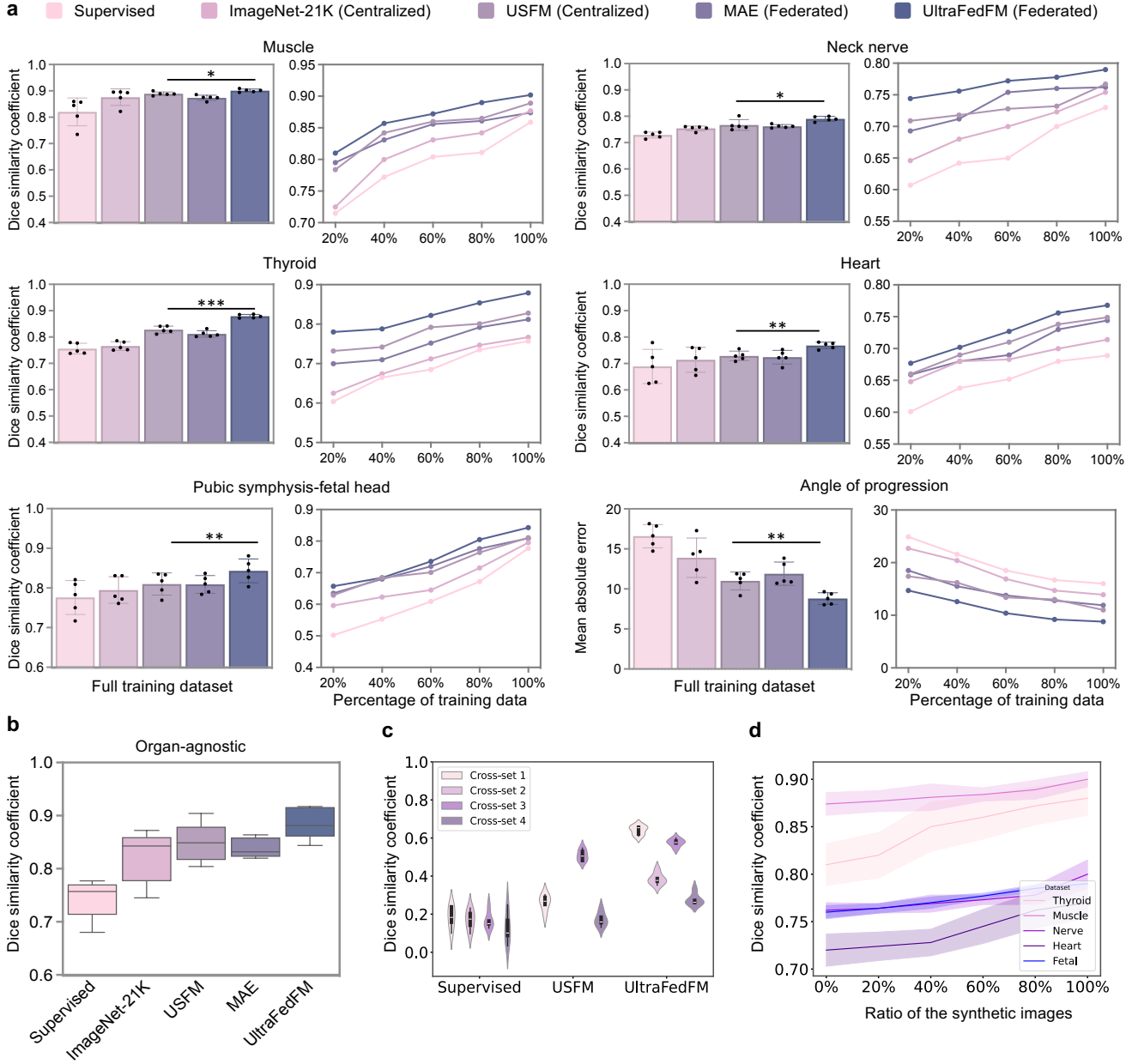


Figure 4. Performance on organ and lesion segmentation. **a** Internal evaluation on six independent segmentation tasks. The histogram is the models fine-tuned on the full data of each dataset, and the line chart is the models fine-tuned on part of the labeled data. For each task, we fine-tuned the model with five different random seeds. The error bars show 95% confidence intervals (CI) of the estimates and the bar center is the mean estimate. We compared the performance using dice similarity coefficient (DSC) score. P -value is calculated with the two-sided t-test among UltraFedFM and the most competitive comparison model. *, **, *** denotes $p < 0.05$, $p < 0.005$, and $p < 0.005$. **b** Performance of UltraFedFM on organ-agnostic dataset fine-tuned with a single decoder. **c** Comparison of cross-institution generalization performance. Cross-set 1 denotes fine-tuning on thyroid dataset and test on muscle dataset; Cross-set 2 denotes fine-tuning on thyroid dataset and test on muscle dataset; Cross-set 3 denotes fine-tuning on muscle dataset and test on thyroid dataset; Cross-set 4 denotes fine-tuning on muscle dataset and test on nerve dataset. The width represents the density of the data points at different values. The central line within each violin indicates the median. **d** Organ and lesion segmentation performance of UltraFedFM on different ratios of real and synthetic ultrasound imaging data. The 95% CI of DSC is plotted in color bands, and the center points of the bands indicate the mean value of DSC.

This success may be attributed to MAE’s ability to learn robust feature representations in images where structures can vary significantly across patients or organs. Clinically, this translates to more accurate diagnostic predictions, especially for complex cases involving subtle lesions or challenging anatomical regions.

The stability of UltraFedFM’s predictions

The stability of model predictions is essential for ensuring reliable clinical decision-making, particularly in ultrasound-based diagnostics where inconsistencies can lead to misdiagnosis. To this end, we quantitatively compared the prediction stability of UltraFedFM with the baseline USFM⁸ under two settings: organ-specific (Fig. 5c) and organ-agnostic (Fig. 5d). USFM shows a broader distribution (mean $\mu = 0.808$ and standard deviation $\sigma = 0.174$). In contrast, UltraFedFM’s predictions concentrate in a high DSC range (mean $\mu = 0.857$ and standard deviation $\sigma = 0.103$). Moreover, stability is paramount when dealing with organs that exhibit significant inter-patient variability, such as the liver or kidneys. Thus, we further introduce random noise to simulate real-world ultrasound imaging perturbations, such as tissue movement, operator variability, or imaging artifacts. We compared the test results under varying levels of noise. Despite these disturbances, UltraFedFM maintained highly correlated test scores (Fig. 5e-f), demonstrating its robustness and reliability in clinical environments where imaging conditions can be unpredictable.

UltraFedFM generalizes to new medical scenarios

Beyond learning ability, a crucial metric to evaluate the practicality of FMs in real-life scenarios is the generalization ability. To assess this, we selected two medical institutions not involved in the pre-training stage (high-frequency skin ultrasound imaging dataset and kidney disease ultrasound imaging dataset). This evaluation aims to determine how well the model performs on unseen ultrasound imaging modalities and organs, both key challenges in ultrasound diagnostics. As shown in Fig. 6. UltraFedFM consistently demonstrates superior generalization across different modalities (Fig. 6a-b), achieving an average AUROC of 0.925, significantly outperforming all other baselines ($p < 0.01$). Fig. 6c shows UltraFedFM’s strong generalization ability to new organs and related diseases, with an AUROC of 0.878 and an average precision (AP) of 0.980. Fig. 6d illustrates that UltraFedFM achieves an AUROC of 97.1% and an AP of 0.910, despite the textural and color differences of high-frequency ultrasound imaging from conventional methods. Such generalization is essential for real-world applications where clinicians frequently encounter new organs or modalities that the training data may not be easily accessed.

Model interpretation

UltraFedFM’s performance on downstream tasks is determined by its feature extraction capabilities. To gain a deep understanding of how UltraFedFM interprets ultrasound images, we qualitatively analyzed the internal mechanisms of the pre-text task of UltraFedFM during pre-training and how UltraFedFM made task-specific decisions on downstream tasks.

During pre-training, the pre-text task enables the model to learn ultrasound-specific context across various ultrasound imaging modalities. As shown in Fig. 6e, UltraFedFM accurately reconstructs images even when large portions are masked. This process allows UltraFedFM to effectively capture the critical anatomical details, such as muscle textures, organ tissues, and lesion structures, which contribute to the performance in downstream tasks. Fig. 6f shows the two ultrasound scanning modes used in the pre-training process, where we applied a scanning mode-aware transformation (SMAT) to balance the dataset. This prevents UltraFedFM from easily overfitting to one scanning mode during fine-tuning, which is essential since ultrasound imaging varies widely depending on the equipment and operator techniques used, and models need to adapt across these variations.

For downstream lesion segmentation tasks, Fig. 6g and Fig. 6h visualize UltraFedFM’s precise localization of salient lesion areas and target boundaries. Clinically, the model’s ability to focus on salient areas while excluding irrelevant background interference (Fig. 6h) enhances its accuracy in detecting complex lesion structures, which is essential for diagnosing diseases with subtle or overlapping symptoms.

Fig. 7 illustrates the embedding feature space of different classes in the fine-tuned model. UltraFedFM demonstrates superior class discrimination, with different classes clearly separated in high-dimensional space, resulting in more precise classification boundaries. This ability is crucial in clinical applications where precise differentiation between pathological and non-pathological tissue can impact treatment decisions. In contrast, the baseline supervised model exhibits weaker differentiation and less distinct classification results. Fig. 8a further shows how UltraFedFM effectively recognizes specific patterns and targets via the attention mechanism. For example, in pancreas, liver, breast, and gallbladder imaging, the model focuses on the center and surrounding areas of tumor lesions. In colorectal and lung imaging, it targets high-density textured regions while ignoring irrelevant hollow regions such as intestines and alveoli. For fetal ultrasound imaging, UltraFedFM focuses on the solid parts of the fetus and excludes irrelevant regions such as the uterus and muscles. In addition, we visualized the evolution of the attention map during pre-training (see Fig. 8b). As pre-training progresses, the local model increasingly focuses on meaningful regions, thereby enhancing the effectiveness of the global model.

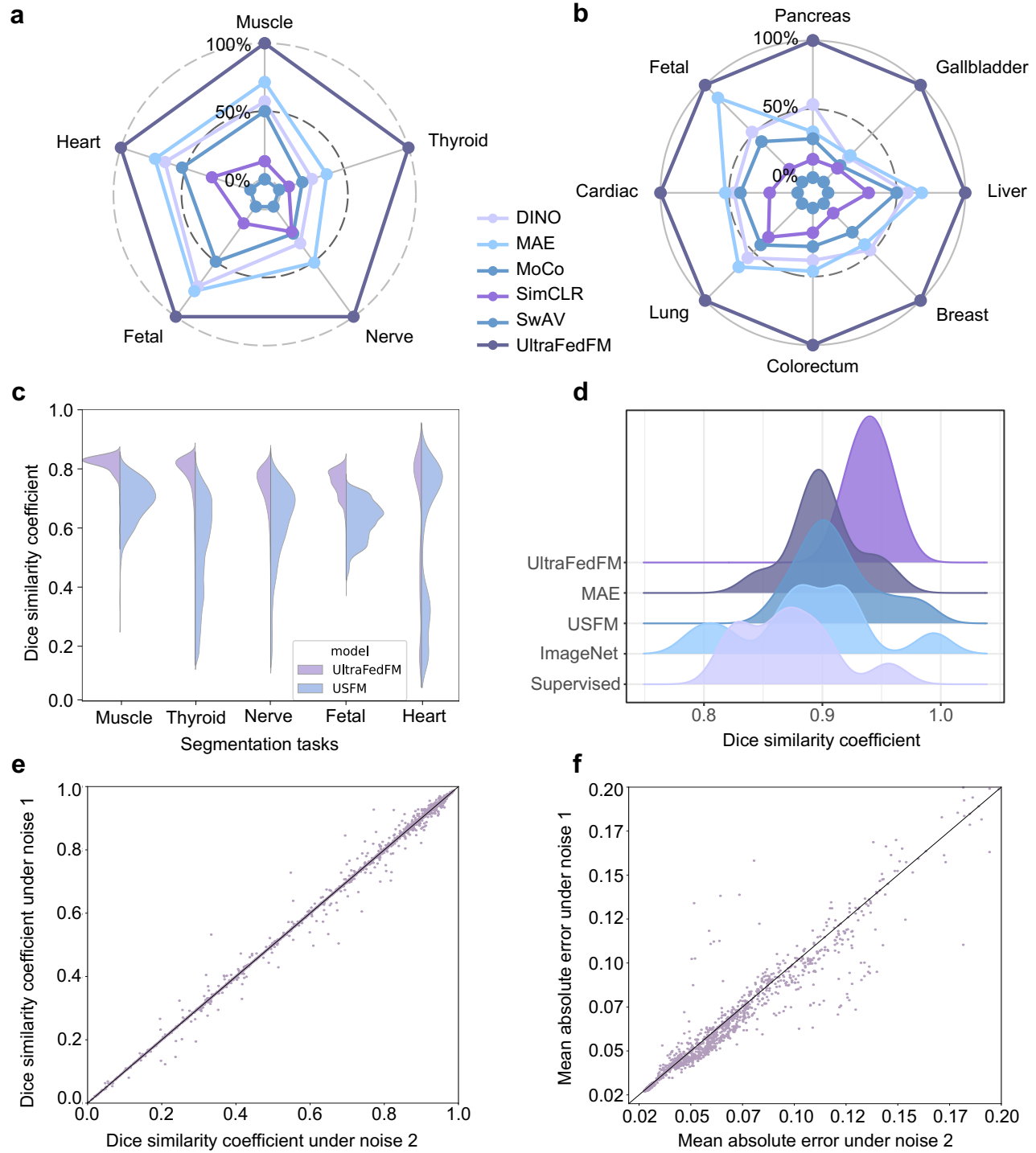


Figure 5. a-b Impact of different self-supervised learning strategies on UltraFedFM for classification and segmentation tasks. All results are scaled and normalized relative to UltraFedFM. Specific quantitative results are available in Supplementary Table 4. **c** Comparison of the prediction distribution between UltraFedFM and USFM across five independent segmentation tasks. UltraFedFM’s predictions are concentrated within a high dice similarity coefficient range (mean $\mu = 0.857$, standard deviation $\sigma = 0.103$), whereas USFM’s predictions show greater dispersion (mean $\mu = 0.808$, standard deviation $\sigma = 0.174$). **d** Prediction distribution of all methods on organ-agnostic segmentation tasks, where UltraFedFM exhibits the best performance. **e-f** Prediction stability of UltraFedFM on lesion segmentation (**e**) and disease classification (**f**) tasks. Random Gaussian blur is applied to the input data to simulate random input distribution variability.

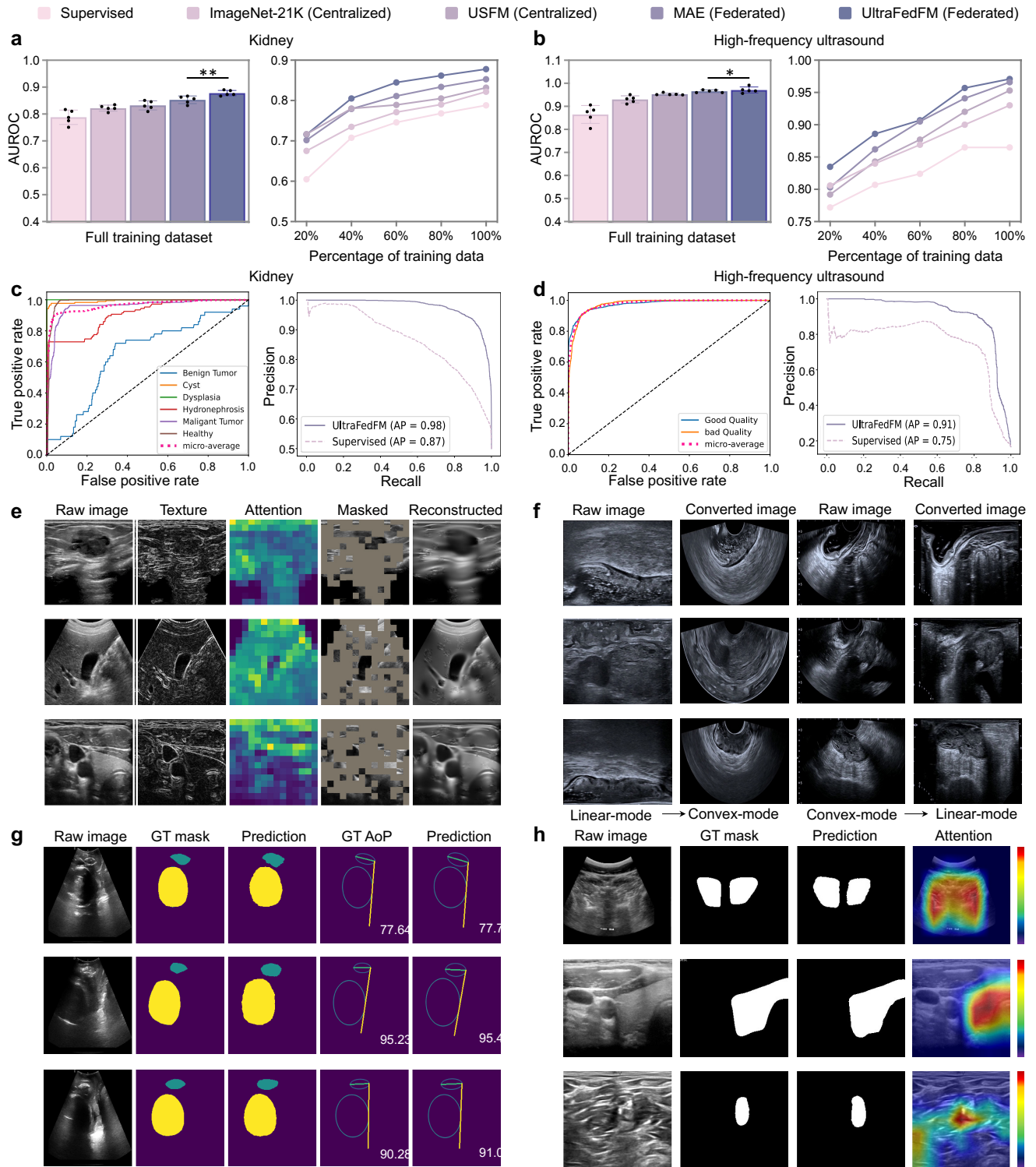


Figure 6. Generalization and Qualitative results of UltraFedFM. **a-b** We compare the generalization performance of different models on out-of-distribution organ (i.e., kidney) and modality (i.e., high-frequency ultrasound), where each model is fine-tuned five times to calculate the average performance. We also assess the performance using a partial fine-tuning set. **c** The receiver operating characteristic curve (ROC) and precision-recall curve (PRC) on a new organ. **d** ROC and PRC on a new ultrasound imaging modality. **e** The reconstructed ultrasound images from the pre-trained model, where the masked regions are selected based on texture information. **f** To increase the richness and balance of features, images captured in linear-array mode and convex-array mode are transformed into each other. **g** Visualization of multi-class organ segmentation and the prediction of the angle of progression (AoP). **h** Visualization of binary lesion segmentation. Heatmaps highlight the attention areas of the features extracted from the pre-trained encoder. The closer the color is to red, the more the model pays attention to the area.

Discussion

With the growing demand for public health solutions, there is an urgent need to develop AI-based foundation models for wide application to real-world clinical scenarios. In this work, targeting the most widely used ultrasound data, we are the first to propose a comprehensive privacy-preserving ultrasound foundation model (USFM) using federated learning, namely UltraFedFM. By eliminating privacy concerns through decentralized pre-training, UltraFedFM leverages large-scale global datasets, enhancing its generalization capabilities. Regarding the above extensive experimental results, UltraFedFM demonstrates excellent performance, favorable generalization and robustness, and good adaptability to fine-tuning data. Specifically, it can handle different clinical tasks, such as diagnosing diseases, segmenting interest of regions (i.e., pathological tissues or organs), and analyzing spatial relationships of fetal organs, making it versatile for a wide range of medical applications. Moreover, UltraFedFM can be fine-tuned in a modality-agnostic manner to enable a single decoder to diagnose multiple diseases present in different modalities. Even with limited fine-tuning data, it consistently outperforms other baseline methods in both accuracy and stability. Across various ultrasound modalities and clinical tasks, UltraFedFM performs with judgment capabilities comparable to human clinicians.

The relations of UltraFedFM with previous achievements. Ultrasound imaging, a widely used clinical diagnostic tool, is renowned for its convenience and accuracy. Previous research in ultrasound diagnostics primarily focused on deep learning models trained on specific ultrasound modalities, targeting the diagnosis or segmentation of disease types within fixed imaging contexts. For example, Antropova et al.²⁴ developed a method that utilized pre-trained CNNs to extract and aggregate features, which were then combined with hand-crafted features from CADx for breast cancer diagnosis. Similarly, Basu et al.⁷ investigated multi-scale and second-order pooling architectures to address false textures in gallbladder ultrasound, achieving precise localization and detection of malignant gallbladder tumors. Jiang et al.²⁵ introduced a sparse computation and temporal fusion architecture designed for the accurate and real-time segmentation of colorectal cancer lesions. These studies have significantly advanced the application of AI in various ultrasound modalities, leading to improvements in automatic ultrasound image analysis, including lesion segmentation, disease diagnosis, and treatment planning. These successes are primarily attributed to the synergistic effects of data, models, and algorithms, specifically the collection and thorough annotation of datasets for specific organs or diseases, as well as specially designed network structures and training methods. However, a critical bottleneck limiting the advancement of medical imaging algorithms is the limited availability of fully annotated medical data.

Medical image annotation demands the expertise of trained physicians, and the segmentation tasks in particular requires substantial time and effort. Traditional methods were often trained on only hundreds or thousands of samples, significantly impacting the models' stability and generalizability in real-world applications. Meanwhile, with the evolution of ultrasound imaging technology, its application to an increasing number of organs and diseases presents challenges for models trained on single-organ or single-disease data, making it difficult to meet expanding clinical demands. There is a growing interest in developing a label-efficient ultrasound model that can be generalized across various tasks and organs, enabling rapid adaptation and deployment in clinical practice.

This led to the introduction of the foundation model (FM) based on self-supervised learning (SSL), which is capable of learning universal features independent of organs and diseases from unlabeled data. Prior to UltraFedFM, several studies explored FMs in medical imaging^{26–30}, covering various modalities such as ophthalmic images, endoscopy, and CT scans. In the field of ultrasound imaging, Christensen et al.⁹ proposed an FM specifically for cardiac ultrasound, pre-trained on over one million echocardiogram videos for diagnosing various heart diseases. Jiao et al.⁸ compiled and organized over two million ultrasound images across 12 different categories to establish a general USFM. However, these foundation models either focus on developing and applying to a single ultrasound modality, which is limited in actual clinical deployment; or require centralized collection and processing of multi-center large-scale data. On the one hand, this approach requires expensive servers to store and process data, and on the other hand, the circulation of data inevitably involves the disclosure of patient information, especially rare disease data, which hinders the development of universal models.

The advantage of UltraFedFM. While UltraFedFM is not the first FM developed for ultrasound imaging, it is the first to integrate privacy protection during the model development process. Previous methods highlighted that, in most cases, private data held by different institutions is not shared, and public data must be anonymized to protect patient privacy, making it challenging to utilize a vast amount of available medical data. In this study, federated learning was used to pre-train the USFM. UltraFedFM was pre-trained on over 1 million ultrasound images from 16 independent institutions worldwide, covering 19 different organs and 10 ultrasound modalities. The model's efficacy was validated on data from more than 12 different types of organs and lesions. UltraFedFM utilizes the most comprehensive pre-training dataset, including emerging ultrasound modalities like contrast-enhanced ultrasound (CEUS), high-frequency ultrasound (HFUS), and endorectal ultrasound (ERUS). Recognizing the different scanning modes produced by various ultrasound probes, an image generation technique based on scan mode conversion was innovatively proposed. This technique augments ultrasound images without the need for additional generative models, effectively doubling the pre-training dataset to 2 million images with balanced representation across scanning modes.

Through careful selection of pre-training image quantity and the design of pre-training algorithms specific to ultrasound imaging, it has been demonstrated for the first time that a distributed pre-training foundation model can achieve comparable performance to centralized foundation models in overall performance across multiple downstream tasks. In ultrasound disease diagnosis tasks, UltraFedFM achieved an average AUROC of 0.927 across eight organs, significantly ($p < 0.001$) surpassing USFM's 0.894 AUROC. In ultrasound lesion segmentation tasks, UltraFedFM achieved an average DSC score of 0.876, significantly ($p < 0.001$) exceeding USFM's 0.858.

The security of UltraFedFM during the pre-training process and its accuracy across various ultrasound imaging applications facilitate the clinical translation of AI technology. Previously, only large institutions with efficient data management workflows could develop FM from vast private medical datasets. This study shows that using a federated learning framework enables the global medical community to leverage diverse and abundant medical data resources to pre-train comprehensive and general FM, and even small-scale data clients with uncommon organs (e.g., Uterus, testis) or modalities (e.g., contrast-enhanced ultrasound, high-frequency ultrasound) can effectively participate in training without worrying about privacy issues, accelerating AI advancement in the medical field. Currently, UltraFedFM's diagnostic and image analysis capabilities have reached levels comparable to those of professional ultrasound physicians in many areas. This can significantly alleviate the pressure on outpatient services and large-scale ultrasound disease screening in regions with high medical demand and limited medical resources, substantially enhancing the work efficiency of ultrasound physicians.

The current limitations of UltraFedFM. While systematically evaluating the advantages of UltraFedFM in ultrasound imaging analysis, this study still has several limitations and unresolved challenges. Firstly, during the federated pre-training process, the quantity and variety of ultrasound image data vary across institutions, resulting in non-independent and identically distributed (non-IID) data. This poses challenges to the aggregation process of models from different institutions. Although a data volume-based balancing method was incorporated to adjust each institution's contribution to the global model during pre-training, the non-IID problem persists and may worsen with more institutions participating in the pre-training. Secondly, while redundancy in the pre-training dataset was reduced, public dataset collection conditions still led to numerous images originating from the same ultrasound video or patient, limiting the diversity of features that the model can learn. It is speculated that by extending UltraFedFM's pre-training framework to collaborate with more global medical institutions and using a more balanced and diverse pre-training dataset, the model's accuracy and generalizability could be further enhanced. Lastly, although UltraFedFM effectively addresses critical clinical diagnostic and segmentation tasks and has been validated across 12 different types of organs and diseases, it does not utilize the vast amount of textual diagnostic reports available in ultrasound examinations. Integrating multimodal features from both text and images could further improve the foundational model's accuracy in various clinical tasks and enable the development of additional clinically useful tasks like question-answering and diagnostic report generation.

The significance and application of UltraFedFM. In conclusion, this study provided a robust and reliable framework for developing comprehensive USFMs. It has been demonstrated that high-performance and stable models can be pre-trained without risking privacy leakage. This breakthrough can significantly advance the development of USFMs and potentially lead to the emergence of more powerful general-purpose medical AI. UltraFedFM has already shown excellent performance in various ultrasound clinical tasks and holds promise for further expansion. It has the potential to replace traditional ultrasound AI diagnostic models and play a crucial role in clinical decision support. The theoretical contributions of this research lie in validating the efficacy of federated learning for pre-training medical FMs, inspiring further academic advancements in the field. Practically, the implementation of UltraFedFM can enhance diagnostic accuracy, streamline clinical workflows, and improve patient outcomes. Additionally, these findings offer valuable insights for policy-making, particularly in the areas of data privacy and the integration of AI in healthcare. By ensuring data privacy and leveraging federated learning, the collective power of global medical data can be harnessed to drive innovations in medical diagnostics and treatment planning, ultimately transforming the healthcare delivery landscape.

References

1. Whitworth, M., Bricker, L. & Mullan, C. Ultrasound for fetal assessment in early pregnancy. *Cochrane database systematic reviews* (2015).
2. Akkus, Z. *et al.* A survey of deep-learning applications in ultrasound: Artificial intelligence-powered ultrasound for improving clinical workflow. *J. Am. Coll. Radiol.* **16**, 1318–1328 (2019).
3. Donofrio, M. T. *et al.* Diagnosis and treatment of fetal cardiac disease: a scientific statement from the american heart association. *Circulation* **129**, 2183–2242 (2014).
4. Feldman, M. K., Katyal, S. & Blackwood, M. S. Us artifacts. *Radiographics* **29**, 1179–1189 (2009).
5. Lin, Z. *et al.* A new dataset and a baseline model for breast lesion detection in ultrasound videos. In *International Conference on Medical Image Computing and Computer-Assisted Intervention*, 614–623 (Springer, 2022).

6. Burgos-Artizzu, X. P. *et al.* Evaluation of deep convolutional neural networks for automatic classification of common maternal fetal ultrasound planes. *Sci. Reports* **10**, 10200 (2020).
7. Basu, S., Gupta, M., Rana, P., Gupta, P. & Arora, C. Surpassing the human accuracy: Gallbladder cancer detection from usg with curriculum learning. In *Proceedings of the IEEE/CVF Conference on Computer Vision and Pattern Recognition (CVPR)*, 20854–20864 (2022).
8. Jiao, J. *et al.* Usfm: A universal ultrasound foundation model generalized to tasks and organs towards label efficient image analysis. *Med. Image Analysis* **96**, 103202 (2024).
9. Christensen, M., Vukadinovic, M., Yuan, N. & Ouyang, D. Vision–language foundation model for echocardiogram interpretation. *Nat. Medicine* 1–8 (2024).
10. Voigt, P. & Von dem Bussche, A. The eu general data protection regulation (gdpr). *A Pract. Guid. 1st Ed., Cham: Springer Int. Publ.* **10**, 10–5555 (2017).
11. He, K. *et al.* Masked autoencoders are scalable vision learners. In *Proceedings of the IEEE/CVF conference on computer vision and pattern recognition*, 16000–16009 (2022).
12. Anna, M. *et al.* Ultrasound nerve segmentation (2016).
13. Luminous database: Lumbar multifidus muscle segmentation from ultrasound. [Online]. <https://users.encs.concordia.ca/~impact/luminous-database/>.
14. Yang, J., Ding, X., Zheng, Z., Xu, X. & Li, X. Graphecho: Graph-driven unsupervised domain adaptation for echocardiogram video segmentation. In *Proceedings of the IEEE/CVF International Conference on Computer Vision*, 11878–11887 (2023).
15. Stanford aimi shared datasets. [Online]. <https://stanfordaimi.azurewebsites.net/datasets/a72f2b02-7b53-4c5d-963c-d7253220bfd5>.
16. Pedraza, L. *et al.* An open access thyroid ultrasound image database. In *10th International symposium on medical information processing and analysis*, vol. 9287, 188–193 (SPIE, 2015).
17. Wunderling, T. *et al.* Comparison of thyroid segmentation techniques for 3d ultrasound. In *Medical Imaging 2017: Image Processing*, vol. 10133, 346–352 (SPIE, 2017).
18. Gong, H. *et al.* Multi-task learning for thyroid nodule segmentation with thyroid region prior. In *2021 IEEE 18th international symposium on biomedical imaging (ISBI)*, 257–261 (IEEE, 2021).
19. Lu, Y. *et al.* The jnu-ifm dataset for segmenting pubic symphysis-fetal head. *Data brief* **41**, 107904 (2022).
20. Chen, T., Kornblith, S., Norouzi, M. & Hinton, G. A simple framework for contrastive learning of visual representations. In *International conference on machine learning*, 1597–1607 (PMLR, 2020).
21. Caron, M. *et al.* Unsupervised learning of visual features by contrasting cluster assignments. *Adv. neural information processing systems* **33**, 9912–9924 (2020).
22. Caron, M. *et al.* Emerging properties in self-supervised vision transformers. In *Proceedings of the IEEE/CVF international conference on computer vision*, 9650–9660 (2021).
23. Chen, X., Xie, S. & He, K. An empirical study of training self-supervised vision transformers. In *Proceedings of the IEEE/CVF international conference on computer vision*, 9640–9649 (2021).
24. Antropova, N., Huynh, B. Q. & Giger, M. L. A deep feature fusion methodology for breast cancer diagnosis demonstrated on three imaging modality datasets. *Med. physics* **44**, 5162–5171 (2017).
25. Jiang, Y. *et al.* Towards a benchmark for colorectal cancer segmentation in endorectal ultrasound videos: Dataset and model development (2024). [2408.10067](https://arxiv.org/abs/2408.10067).
26. Zhou, Y. *et al.* A foundation model for generalizable disease detection from retinal images. *Nature* **622**, 156–163 (2023).
27. Qiu, J. *et al.* Visionfm: a multi-modal multi-task vision foundation model for generalist ophthalmic artificial intelligence. *arXiv preprint arXiv:2310.04992* (2023).
28. Wang, Z., Liu, C., Zhang, S. & Dou, Q. Foundation model for endoscopy video analysis via large-scale self-supervised pre-train. In *International Conference on Medical Image Computing and Computer-Assisted Intervention*, 101–111 (Springer, 2023).
29. Hamamci, I. E. *et al.* A foundation model utilizing chest ct volumes and radiology reports for supervised-level zero-shot detection of abnormalities. *arXiv preprint arXiv:2403.17834* (2024).

30. Pai, S. *et al.* Foundation model for cancer imaging biomarkers. *Nat. Mach. Intell.* (2024).
31. Petrusca, L. *et al.* Hybrid ultrasound/magnetic resonance simultaneous acquisition and image fusion for motion monitoring in the upper abdomen. *Investig. radiology* **48**, 333–340 (2013).
32. De Luca, V., Tschannen, M., Székely, G. & Tanner, C. A learning-based approach for fast and robust vessel tracking in long ultrasound sequences. In *Medical Image Computing and Computer-Assisted Intervention–MICCAI 2013: 16th International Conference, Nagoya, Japan, September 22–26, 2013, Proceedings, Part I* **16**, 518–525 (Springer, 2013).
33. Ouyang, D. *et al.* Video-based ai for beat-to-beat assessment of cardiac function. *Nature* **580**, 252–256 (2020).
34. Burgos-Artizzu, X. P. *et al.* FETAL_PLANES_DB: Common maternal-fetal ultrasound images. <https://doi.org/10.5281/zenodo.3904280> (2020).
35. Tumor detection, segmentation and classification challenge on automated 3d breast ultrasound (abus) 2023. [Online]. <https://tdsc-abus2023.grand-challenge.org/Organizers/>.
36. Duque, V. G. *et al.* Ultrasound segmentation analysis via distinct and completed anatomical borders. *Int. J. Comput. Assist. Radiol. Surg.* 1–9 (2024).
37. Liang, X., Cao, Q., Huang, R. & Lin, L. Recognizing focal liver lesions in contrast-enhanced ultrasound with discriminatively trained spatio-temporal model. In *2014 IEEE 11th International Symposium on Biomedical Imaging (ISBI)*, 1184–1187 (IEEE, 2014).
38. Liang, X., Lin, L., Cao, Q., Huang, R. & Wang, Y. Recognizing focal liver lesions in ceus with dynamically trained latent structured models. *IEEE Transactions on Med. Imaging* **35**, 713–727 (2015).
39. Leclerc, S. *et al.* Deep learning for segmentation using an open large-scale dataset in 2d echocardiography. *IEEE transactions on medical imaging* **38**, 2198–2210 (2019).
40. Covid-blues. [Online]. <https://github.com/NinaWie/COVID-BLUES>.
41. Li, J., Zhang, P., Wang, T., Wang, K. & Sheng, B. Lepset. In <https://doi.org/10.5281/zenodo.8041285>, DOI: [10.5281/zenodo.8041285](https://doi.org/10.5281/zenodo.8041285) (2023).
42. Prabakaran, B. S., Hamelmann, P., Ostrowski, E. & Shafique, M. Fpus23: an ultrasound fetus phantom dataset with deep neural network evaluations for fetus orientations, fetal planes, and anatomical features. *IEEE Access* **11**, 58308–58317 (2023).
43. Basu, S., Gupta, M., Madan, C., Gupta, P. & Arora, C. Focusmae: Gallbladder cancer detection from ultrasound videos with focused masked autoencoders. In *Proceedings of the IEEE/CVF Conference on Computer Vision and Pattern Recognition*, 11715–11725 (2024).
44. Al-Dhabyani, W., Gomaa, M., Khaled, H. & Fahmy, A. Dataset of breast ultrasound images. *Data brief* **28**, 104863 (2020).
45. Born, J. *et al.* Accelerating detection of lung pathologies with explainable ultrasound image analysis. *Appl. Sci.* **11**, 672 (2021).
46. Czajkowska, J., Juszczak, J., Piejko, L. & Glenc-Ambroży, M. High-frequency ultrasound dataset for deep learning-based image quality assessment. *Sensors* **22**, 1478 (2022).
47. Gong, H. *et al.* Thyroid region prior guided attention for ultrasound segmentation of thyroid nodules. *Comput. biology medicine* **155**, 106389 (2023).
48. Belasso, C. J. *et al.* Luminous database: lumbar multifidus muscle segmentation from ultrasound images. *BMC Musculoskelet. Disord.* **21**, 1–11 (2020).

Table 1. Summary of the pre-training datasets and the data distributions of all local clients.

Clients	Nmae	Location	Main US Madality	Main Organ	Numbers
Client 1	BUV ⁵	Hong Kong, China	Superficial	Breast	25,727
Client 2	CLUST ^{31,32}	Switzerland	Abdominal	Liver	35,626
Client 3	EchoNet-Dynamic ³³	California, USA	Echocardiogram	Heart	150,243
Client 4	FETAL-PLANES ^{6,34}	Spain	Fetal	Fetal organs	12,400
Client 5	TDSC-ABUS ³⁵	Harbin, China	3D Abdominal	Breast	126,918
Client 6	Leg-3D-US ³⁶	German	3D Muscle	Muscle	115263
Client 7	Thyroid Ultrasound Cine-clip ¹⁵	California, USA	Superficial	Thyroid	17,412
Client 8	SYSU-FLL-CEUS ^{37,38}	Guangzhou, China	Abdominal	Liver	118,485
Client 9	CAMUS ³⁹	France	Echocardiogram	Heart	21,214
Client 10	COVID-BLUES ⁴⁰	United Kingdom	Lung	Lung	42,226
Client 11	NerveUS ¹²	Georgia, USA	Superficial	Nerve	11,143
Client 12	LEPset ⁴¹	Chongqing, China	Abdominal	Pancreas	11,499
Client 13	FPUS ⁴²	Austria	Maternal-fetal	Fetal organs	20,378
Client 14	GBUSV ⁴³	India	Abdominal	Gallbladder	10,553
Client 15	ERUS	Sichuan, China	Endorectal	Colorectum	63,426
Client 16	PrivateUS	Sichuan, China	Abdominal, Maternal-fetal, Superficial, Echocardiogram	Uterus, Vascular, Stomach, Spleen, Prostate, Testis, Paratod Gland, Lymph Nodes	235,633

Table 2. Summary of the downstream tasks and the fine-tuning dataset distributions.

Challenge	Location	Modality	Organ	Name	Classes	Train	Test
Classification							
Malignant Cancer Diagnose	Chongqin, China	Endoscopic	Pancreas	LEPset ⁴¹	Benign tumor, Malignant tumor	2,800	700
	Guangzhou, China	Abdominal	Liver	SYSU-CEUS ^{37,38}	Hepatocellular carcinoma, Hemangioma, Focal nodular hyperplasia	10,910	2,728
	India		Gallbladder	GBCU ⁷	Normal tumor, Benign tumor, Malignant tumor	2,292	573
	Egypt	Superficial	Breast	BUS ⁴⁴ , BUV ⁵	Normal tumor, Benign tumor, Malignant tumor	1,119	300
Cancer Infiltration depth staging	Sichuan, China	Endorectal	Colorectum	ERUS	Colorectal tumor staging: T1,T2,T3,T4,T5	1,239	304
Organ disease diagnosis	Sichuan, China	Echocardiogram	Heart	EUS	Patent ductus arteriosus, Atrial septal defect, Ventricular septal defect, Heart valve disease	10,368	2,592
	Sichuan, China	Abdominal	Kidney	KUS	Normal, Cyst, Hydronephrosis, Dysplasia, Benign tumor, Malignant tumor,	5,662	1,415
Covid-19 prediction	United Kingdom	Lung	Lung	POCUS ⁴⁵	Normal, COVID-19, Bacterial pneumonia, Viral pneumonia	3,755	939
Fetal plane recognition	Spain	Maternal-fetal	Fetal Organ	FETAL PLANES ^{6,34}	Abdomen, Brain, Femur, Thorax, Maternal cervix, Other	15,623	3,906
Ultrasound imaging quality assessment	Poland	High-frequency	Skin	HFUS ⁴⁶	Good skin quality, Bad skin quality	13,940	3,485
Segmentation							
Critical organ segmentation	Georgia, USA	Superficial	Brachial plexus	NUS ¹²	Brachial plexus, Background	1,877	446
Lesion segmentation	Guangzhou, China		Thyroid	DDTI ¹⁶ , Thyroid Cine-Clip ¹⁵ , TG3k ¹⁷ , TN3k ^{18,47}	Thyroid nodule, Background	20,109	5,027
Muscle segmentation	Montreal, Canada	Muscle	Lumbar multifidus muscle	LUMINOUS ⁴⁸	Muscle, Background	276	65
Heart ventricle segmentation	Guangzhou, China	Echocardiogram	Heart	CardiacUDA ¹⁴	Left ventricle Right ventricle pulmonary artery left atrium right atrium Background	276	65
Fetal head descent & Progression assessment	Wuhan, China	Transperineal	Pubic & Fetal head	JNU-IFM ¹⁹	Pubic symphysis, Fetal head, Background	2,571	643

Table 3. Summary of the downstream organ-agnostic dataset distributions

Task	Classes	Name	Train	Test
Organ-agnostic disease diagnosis	Pancreatic malignant tumor	LEPset ⁴¹	11,670	3,177
	Gallbladder malignant tumor	GBCU ⁷		
Organ-agnostic lesion segmentation	Liver hepatocellular carcinoma	SYSU-CEUS ³⁷	44,506	11,076
	Breast malignant tumor	BUS ⁴⁴ , BUV ⁵		
	Kidney malignant tumor	KUS		
	Colorectal T4-stage tumor	ERUS		
	Cardiac valve disease	EUS		
	Lung Covid-19	POCUS ⁴⁵		
	Thyroid Nodule	Thyroid Cine-clip ¹⁵ , DDTI ¹⁶ , TG3k ¹⁷ , TN3k ¹⁸		
	Brachial plexus	NUS ¹²		
	Muscle	LUMINOUS ⁴⁸		
	Heart ventricle	CardiacUDA ¹⁴		
	Background			

Table 4. Specific quantitative results of different self-supervised methods

	SimCLR	SwAV	MoCo	DINO	MAE	UltraFedFM
Classification (AUROC)						
Pancreas	0.862	0.854	0.871	0.886	0.874	0.914
Gallbladder	0.867	0.852	0.870	0.879	0.881	0.957
Liver	0.664	0.622	0.693	0.704	0.719	0.764
Breast	0.858	0.851	0.872	0.885	0.881	0.922
Colon	0.827	0.811	0.836	0.845	0.852	0.900
Lung	0.938	0.912	0.944	0.954	0.961	0.987
Heart	0.887	0.865	0.91	0.915	0.922	0.973
Fetal	0.917	0.905	0.943	0.952	0.984	0.996
Segmentation (DSC)						
Muscle	0.817	0.804	0.853	0.860	0.874	0.902
Thyroid	0.781	0.773	0.792	0.800	0.812	0.879
Nerve	0.746	0.733	0.747	0.752	0.762	0.790
Fetal head	0.725	0.704	0.773	0.804	0.810	0.842
Heart	0.704	0.677	0.725	0.737	0.744	0.768

Table 5. Average accuracy score of UltraFedFM across 8 diseases, and comparison with the results of seven ultrasonograph clinicians

Disease class	UltraFedFM	Clinician-A	Clinician-B	Clinician-C	Clinician-D	Clinician-E	Clinician-F	Clinician-G
Breast malignant tumor	0.900	0.600	1.000	0.700	0.800	0.800	0.700	1.000
Kidney malignant tumor	1.000	0.900	0.800	1.000	0.800	0.800	1.000	0.800
Liver hepatocellular carcinoma	1.000	0.833	0.750	0.916	0.500	0.833	0.833	0.750
Gallbladder malignant tumor	0.800	0.100	0.200	0.300	0.600	0.400	0.100	0.500
Pancreatic malignant tumor	0.875	0.250	0.250	0.375	0.375	0.625	0.375	0.375
Colorectal T4 stage tumor	0.900	0.800	0.600	0.700	0.700	0.600	0.600	0.500
Cardiac valve disease	0.700	0.800	0.600	0.600	0.700	0.700	0.800	0.700
Lung Covid-19	0.900	0.900	0.700	0.700	0.700	0.700	0.700	0.900

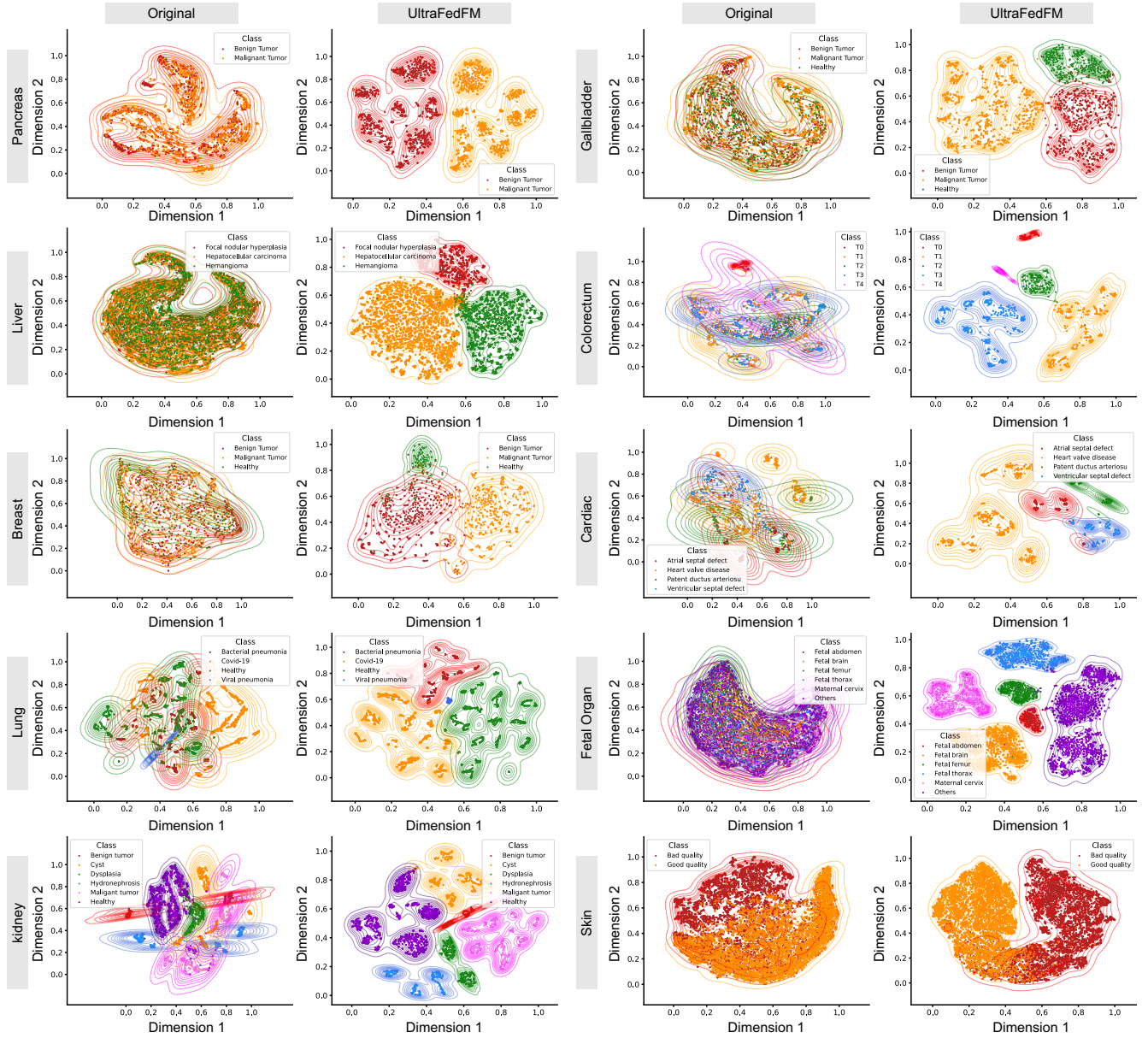


Figure 7. Visualization of the features space. Features from the foundation model and baseline model are extracted on the 10 independent disease diagnosis tasks using the tSNE dimensionality reduction approach. The x-axis corresponds to dimension 1, and the y-axis corresponds to dimension 2 of the reduced feature space. The density contours of each class are underlaid to highlight separability between classes in the feature space.

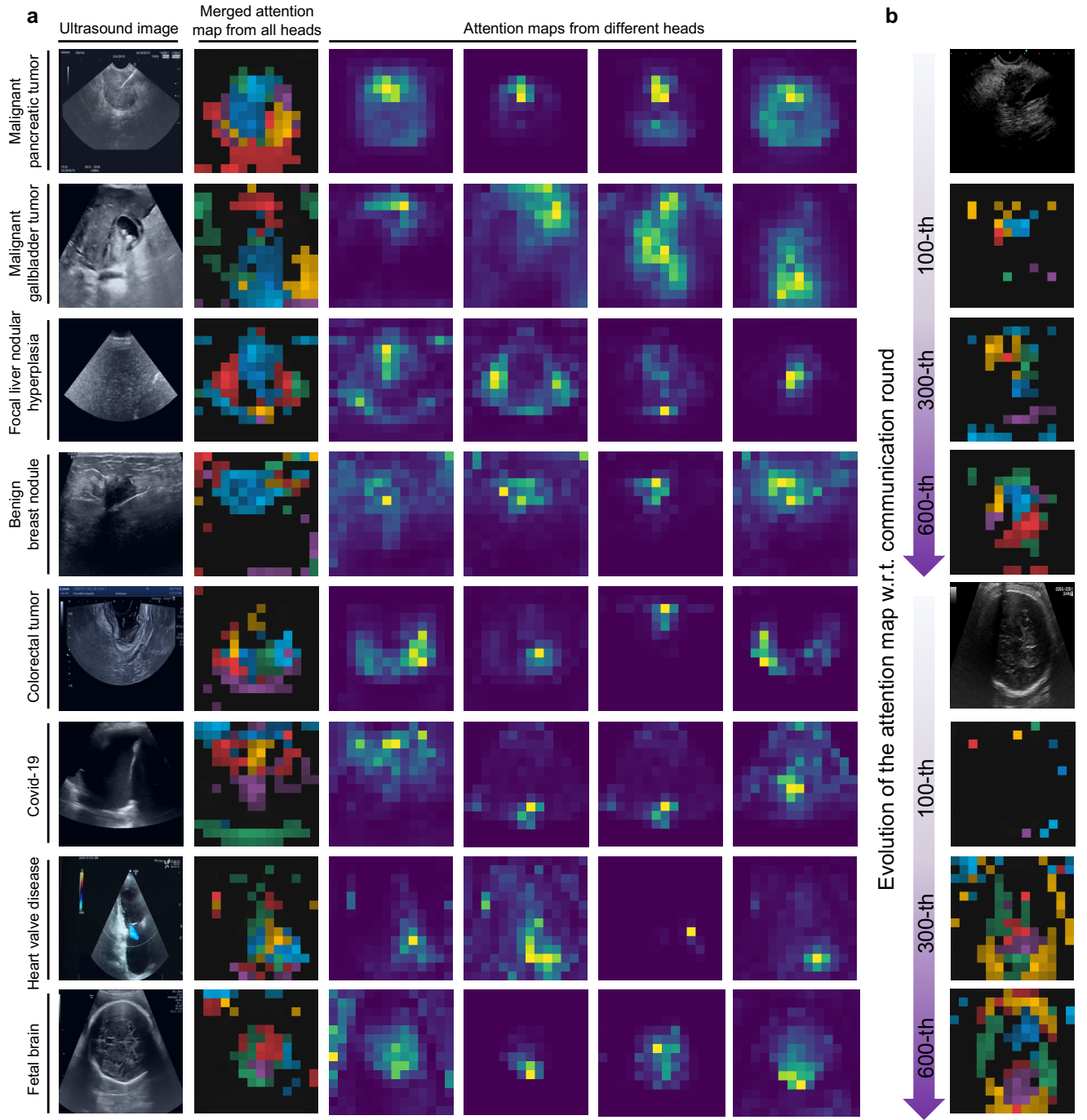
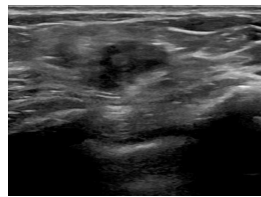
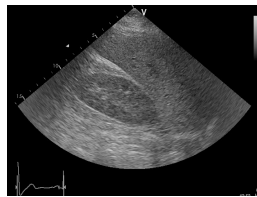


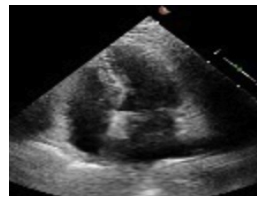
Figure 8. Visualization of the attention map. Explainability of the learned ultrasound image representations of UltraFedFM. **a** Attention maps of different heads of UltraFedFM on images of different organs are visualized. **b** Evolution of attention maps with respect to communication rounds during the federated pre-training.



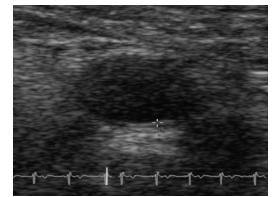
Client 1: Breast



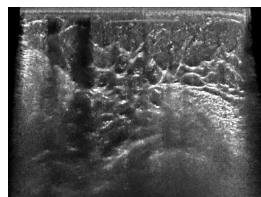
Client 2: Liver



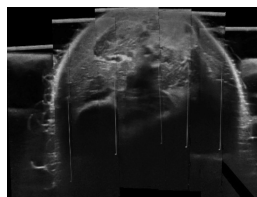
Client 3: Heart



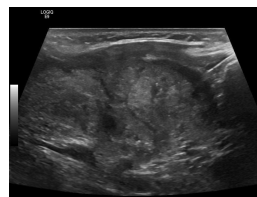
Client 4: Fetal



Client 5: Breast



Client 6: Muscle



Client 7: Thyroid



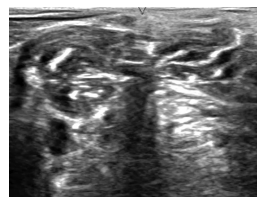
Client 8: Liver



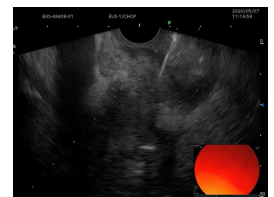
Client 9: Heart



Client 10: Lung



Client 11: Nerve



Client 12: Pancreas



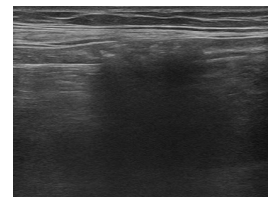
Client 13: Fetal



Client 14: Gallbladder



Client 15: Colorectum



Client 16: Abdominal

Figure 9. Sample images of each client in the pre-training dataset.



Figure 10. Sample images of each category in the downstream validation dataset. The categories in the color blocks are used to construct the organ-agnostic dataset.

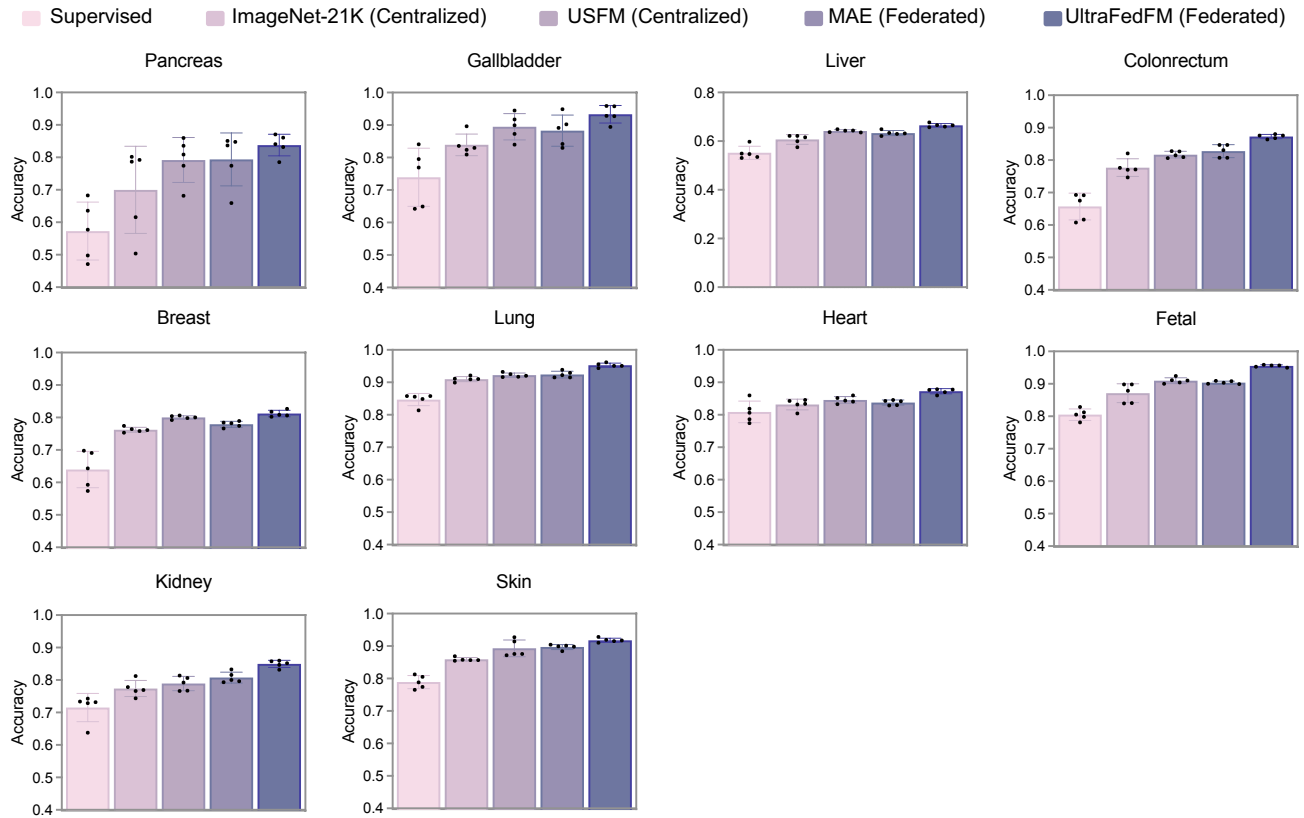


Figure 11. Performance (Accuracy) on systemic disease diagnosis. For each task, we trained the model with 5 different random seeds, determining the shuffling of training data, and evaluated the models on the test set to get 5 replicas. We derived the statistics with the 5 replicas. The error bars show 95% confidence intervals and the bars' center represents the mean value of the accuracy.

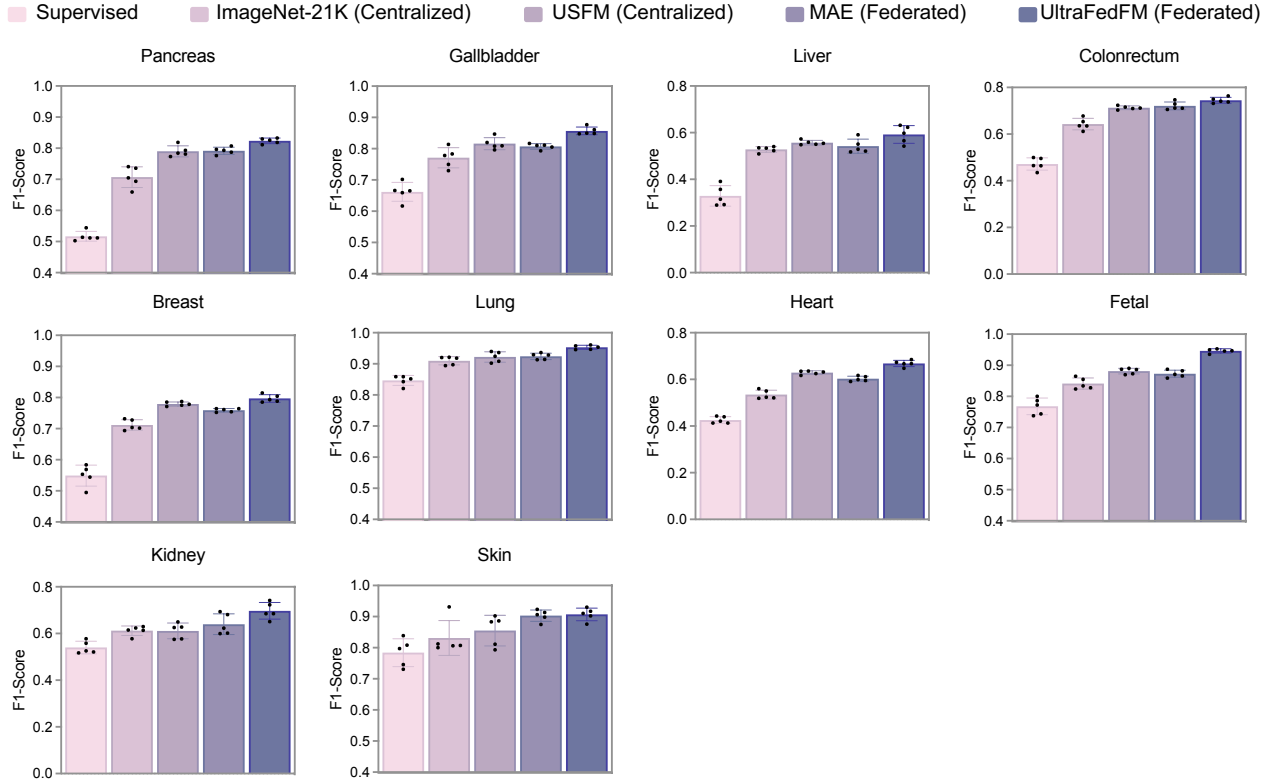


Figure 12. Performance (F1-score) on systemic disease diagnosis. For each task, we trained the model with 5 different random seeds, determining the shuffling of training data, and evaluated the models on the test set to get 5 replicas. We derived the statistics with the 5 replicas. The error bars show 95% confidence intervals and the bars' center represents the mean value of the f1-score.

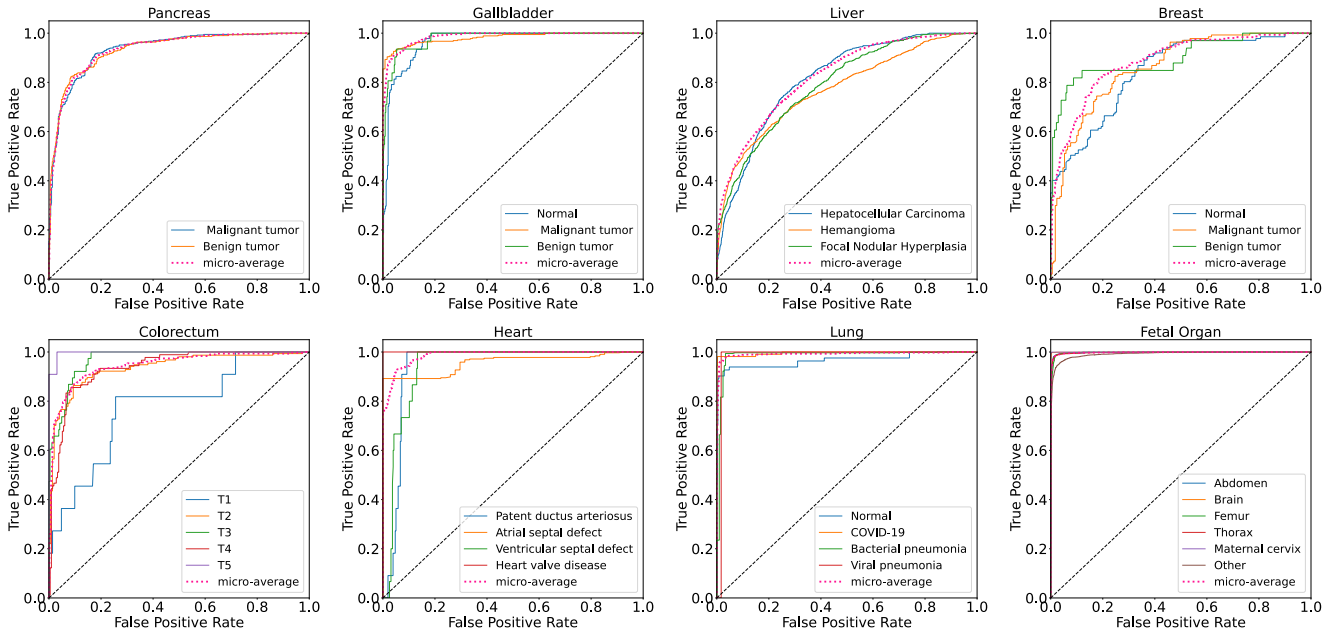


Figure 13. ROC of UltraFedFM on each systemic disease diagnosis tasks.

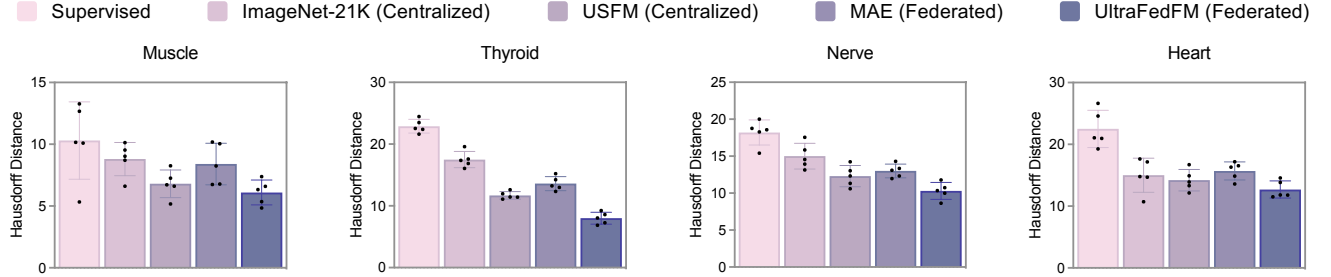


Figure 14. Performance (Hausdorff Distance) on organ and lesion segmentation. For each task, we trained the model with 5 different random seeds, determining the shuffling of training data, and evaluated the models on the test set to get 5 replicas. We derived the statistics with the 5 replicas. The error bars show 95% confidence intervals and the bars' center represents the mean value of the f1-score.

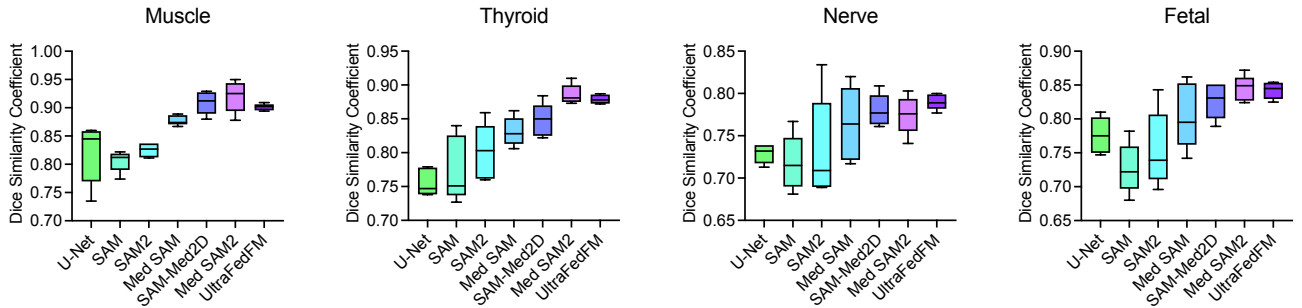


Figure 15. Performance (Dice similarity coefficient) comparison of SAM-based models and UltraFedFM on organ and lesion segmentation. For each task, we trained the model with 5 different random seeds, determining the shuffling of training data, and evaluated the models on the test set to get 5 replicas. We derived the statistics with the 5 replicas. The error bars show 95% confidence intervals and the bars' center represents the mean value of the Dice similarity coefficient.